Biochemical characterization of the respiratory syncytial virus N^0-P complex in solution

Received for publication, October 29, 2018, and in revised form, December 21, 2018 Published, Papers in Press, January 9, 2019, DOI 10.1074/jbc.RA118.006453

Camille Esneau[‡1], Bertrand Raynal[§], Pierre Roblin[¶‖], Sébastien Brûlé[§], Charles-Adrien Richard[‡], Jenna Fix[‡], Jean-François Eléouët[‡2], and Marie Galloux[‡3]

From the [‡]Untié de Virologie et Immunologie Moléculaires, Institut National de la Recherche Agronomique, Université Paris-Saclay, 78350 Jouy-en-Josas, France, [§]Plate-forme de Biophysique Moléculaire, C2RT, Institut Pasteur, 25 Rue du Docteur Roux, 75015 Paris, France, [¶]Synchrotron SOLEIL, L'Orme des Merisiers, F-91410 Saint Aubin, France, and [‖]Laboratoire de Génie Chimique, Université Paul Sabatier, UMR 5503, Toulouse, France

Edited by Charles E. Samuel

As all the viruses belonging to the *Mononegavirales* order, the nonsegmented negative-strand RNA genome of respiratory syncytial virus (RSV) is encapsidated by the viral nucleoprotein N. N protein polymerizes along the genomic and anti-genomic RNAs during replication. This requires the maintenance of the neosynthesized N protein in a monomeric and RNA-free form by the viral phosphoprotein P that plays the role of a chaperone protein, forming a soluble N^0-P complex. We have previously demonstrated that residues 1–30 of P specifically bind to N^0. Here, to isolate a stable N^0-P complex suitable for structural studies, we used the N-terminal peptide of P (P40) to purify truncated forms of the N protein. We show that to purify a stable N^0-P–like complex, a deletion of the first 30 N-terminal residues of N ($N_{\Delta 30}$) is required to impair N oligomerization, whereas the presence of a full-length C-arm of N is required to inhibit RNA binding. We generated structural models of the RSV N^0-P with biophysical approaches, including hydrodynamic measurements and small-angle X-ray scattering (SAXS), coupled with biochemical and functional analyses of human RSV (hRSV) $N_{\Delta 30}$ mutants. These models suggest a strong structural homology between the hRSV and the human metapneumovirus (hMPV) N^0-P complexes. In both complexes, the P40-binding sites on N^0 appear to be similar, and the C-arm of N provides a high flexibility and a propensity to interact with the N RNA groove. These findings reveal two potential sites to target on N^0-P for the development of RSV antivirals.

Human respiratory syncytial virus (hRSV)[4] is the leading cause of severe respiratory tract infections in newborn children worldwide (1). hRSV infects close to 100% of infants within the first 2 years of life. It is the main cause of bronchiolitis in young children, as well as a significant cause of severe respiratory infections in the elderly. The virus belongs to the *Mononegavirales* order and *Pneumoviridae* family (2). Like all the viruses belonging to this order, the hRSV genome is a nonsegmented negative-strand RNA. This genome of 15 kb is enwrapped by the nucleoprotein (N), forming a helical nucleocapsid (3, 4). The crystal structures of the *Mononegavirales* N proteins complexed with RNA show that they all present a similar structural organization with two globular domains (N_{NTD} and N_{CTD}) that form the RNA groove, and N- and C-arms that are involved in N oligomerization (5). The ribonucleoprotein complex constitutes the template for viral transcription and replication by the viral RNA-dependent RNA polymerase (reviewed in Ref. 6; 7). During the viral cycle, the constant supply of neosynthesized monomeric and RNA-free N protein (named N^0) constitutes a prerequisite during replication to encapsidate neosynthesized single-stranded genomic RNA (−RNA) and anti-genomic RNA (+RNA). By analogy with paramyxoviruses and rhabdoviruses, the hRSV P protein plays the role of a chaperone protein by preventing N from binding to cellular RNAs and N self-oligomerization (5, 8, 9). Invariably, the N-terminal residues of P are sufficient to maintain the N^0 form. However, the structure of the RSV N^0-P complex still remains to be solved, and those from related viruses revealed a specificity of P binding at the surface of N proteins that highlighted different mechanisms of the chaperone activity of P. For the vesicular stomatitis virus, N^0-P complex, the residues 11–35 of P adopt an α-helical conformation upon binding to the surface of N, and this binding domain overlaps both the RNA-binding groove and the binding surface of the N_{i+1} N-arm involved in N oligomerization (10). The crystal structures of the Nipah and measles N^0-P complexes show that the P peptide folds into two short helices that bind on the N_{CTD} (11, 12). In these complexes, P binding prevents N from self-oligomerization and maintains it in an open conformation that impairs the interaction with RNA. A similar mechanism was found for the N^0-P of Ebola and Marburg viruses, although the P peptide does not bind at the top of the N_{CTD} but near the RNA groove, and adopts a specific conformation with two short helices (13, 14). More recently, the structure of the N^0-P complex of parainfluenza 5 (PIV5) showed that the binding of the P peptide to the N_{CTD} blocks both the sites

This work was supported by the French Agence Nationale de la Recherche, specific program ANR Blanc 2013 "Respisyncycell" ANR-13-IVS3-0007. The authors declare that they have no conflicts of interest with the contents of this article.

This article contains Table S1.

[1] Present address: Hunter Medical Research Institute, New Lambton Heights NSW 2305, Australia.

[2] To whom correspondence may be addressed. Tel.: 33-1-34-65-26-40; Fax: 33-1-34-65-26-21; E-mail: jean-françois.eleouet@inra.fr.

[3] To whom correspondence may be addressed. Tel.: 33-1-34-65-26-10; Fax: 33-1-34-65-26-21; E-mail: marie.galloux@inra.fr.

[4] The abbreviations used are: hRSV, human respiratory syncytial virus; N, nucleoprotein; P, phosphoprotein; RSV, respiratory syncytial virus; hMPV, human metapneumovirus; TEV, tobacco etch virus; IB, inclusion body; SAXS, small angle X-ray scattering; AUC, analytical ultracentrifugation; CTD, C-terminal domain; NTD, N-terminal domain.

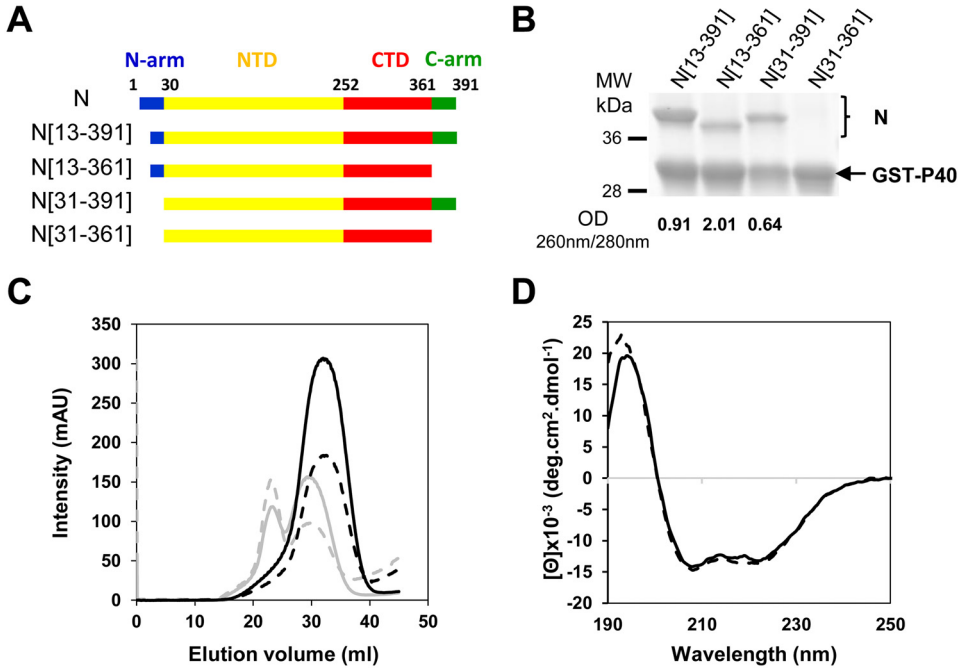

Figure 1. Purification and characterization of truncated N recombinant proteins. *A*, schematic representation of the primary sequence of N and of the different deletions generated. The subdomains of N are colored: N-arm (*blue*), N_{NTD} (*yellow*), N_{CTD} (*red*), and C-arm (*green*). Numbers indicate amino acid positions. *B*, SDS-PAGE analysis of co-purification of GST-P40 and truncated N proteins; the $A_{260\ nm}/A_{280\ nm}$ ratio indicating the presence or absence of RNA is indicated for each sample down the lanes. *C*, elution profiles of N(13–391) (*gray*) and N(31–391) (*black*) from gel filtration, at 280 nm (*solid lines*) and 260 nm (*dash lines*). *D*, far-UV CD spectra showing the absence of major conformational changes between N-RNA rings (*dash lines*) and monomeric N(31–391)-P40 (*solid lines*).

involved in the binding of RNA and of the N-arm of N_{i+1} required for oligomerization, maintaining N in an open conformation (15). Finally, the 3D structure of the human metapneumovirus (hMPV) N^0-P complex, that is phylogenetically the closest virus relative to hRSV, revealed that P binds on the N_{CTD} but also that the C-arm of N presents a specific conformation to block the accessibility to RNA (16).

For RSV, using an N mutant that does not interact with RNA, we have previously shown that the residues 1–30 of P are involved in the chaperone activity (17). The periodicity of the residues critical for N binding also suggests that residues 13–28 of P would adopt a helical conformation upon binding to N. This hypothesis was recently supported by NMR studies of RSV P that revealed the presence of a transient α-helix from Asp-12 to Ile-24 (18). However, the poor stability of the N mutant did not allow us to perform structural studies of the complex.

In this work, we rationally designed deletions of the N- and C-arms of the RSV N protein to destabilize the oligomeric organization of N-RNA rings to purify a stable N^0-P–like complex, when co-expressed with the N-terminal part of P (P40). Using biochemical and biophysical approaches, we obtained structural information about this complex in solution. Our results highlight a strong structural homology between the hMPV and hRSV N^0-P complexes.

Results

Purification of a stable RSV N⁰-P–like complex

We have previously shown that a surrogate of the RSV N^0-P complex can be obtained by co-expression of a K170A/R185A double N mutant with the N terminus of P in bacteria (17). However, the poor stability of this complex at high concentration impaired further structural characterization. Previous studies have shown that the deletion of the 12 N-terminal residues of N, that correspond to nearly half of the N-arm of N, was sufficient to purify a monomeric RNA-free N protein (19, 20). On the other hand, except for hMPV (16), the available crystal structures of N^0-P complexes of *Mononegavirales* were obtained by deleting either the entire N-arm or both N- and C-arms of N (10–15). Based on these data, we decided to generate truncated N proteins deleted of either N-arm or both the N- and C-arms (Fig. 1*A*) to seek for a stable N^0 recombinant protein. Mutant N proteins were co-expressed in *Escherichia coli* with GST-P40 (40 N-terminal residues of P) and purified on GSH-Sepharose beads by affinity chromatography. Among the four N expression constructs that were tested, only the N protein deleted of both N- and C-arms was not co-purified with GST-P40 (Fig. 1*B*). To further characterize the purified N-P complexes, the GST tag was cleaved by TEV protease. We first checked the absence of RNA associated with the isolated recombinant proteins by measuring the $A_{260\ nm}/A_{280\ nm}$ absorption ratio. Whereas these ratios were <1 for N(13–391) and N(31–391), it was close to 2 for N(13–361), showing a strong tendency to associate with nucleic acids for this construct. These observations strongly suggest that the C-arm of N is required to prevent binding of N to RNA during the formation of the N^0-P complex.

The purified recombinant N(13–391)-P40 and N(31–391)-P40 complexes were then analyzed by size exclusion chromatography. The N(31–391)-P40 complex eluted from the column as a single peak that corresponds to an apparent molecular

mass of ~50 kDa (extrapolated from S200 calibration profile), and the $A_{260\,nm}/A_{280\,nm}$ value <1 confirmed the absence of RNA (Fig. 1*C*). For the N(13–391)-P40 complex, in addition to the peak of N protein with apparent molecular mass of ~50 kDa and RNA free, a second peak with an apparent molecular mass of ~500 kDa probably associated to RNA ($A_{260\,nm}/A_{280\,nm}$ >1) corresponding to N-RNA oligomers was obtained (Fig. 1*C*). These results reveal that deletion of the entire N-arm of N is required to obtain a stable monomeric N^0-P complex surrogate. Finally, the secondary structure of the recombinant purified N(31–391)-P40 complex was analyzed by circular dichroism (CD). As shown in Fig. 1*D*, the far-UV CD spectra of the N^0-P complex surrogate was similar to the spectra of the N-RNA rings; both CD traces presented a positive Cotton effect at 190 nm and two negative peaks at 208 and 222 nm, typical of secondary structures with a mainly α-helical content. This result confirms that no major secondary structure change occurs in the N^0 variant when compared with the N-RNA state, as previously shown (17).

Altogether, our data show that the RSV N(31–391) recombinant protein, subsequently named $N_{\Delta 30}$, co-purified with the peptide P40, is a functional surrogate of the RSV N^0-P complex. The $N_{\Delta 30}$-P40 complex was also found to be monomeric upon concentration. Furthermore, our results strongly suggest that the C-arm of N plays a major role in preventing N binding to RNA.

Investigation of the P40-binding site at the surface of the N protein by site-directed mutagenesis

We then tried to identify the binding site of P40 on monomeric N. By analogy with the structure of N^0-P complexes of other *Mononegavirales*, it is expected that P plays a chaperone activity by binding to a surface of N that overlaps with the fixation site of the N-arm of the N_{i+1} protomer within the nucleocapsid, thus impairing N oligomerization. The recent structural elucidation of the hMPV N^0-P complex revealed that P binding also competes with the C-arm of the N_{i-1} protomer involved in oligomerization (Fig. 2*A*) (16). Based on these data and on the structure of RSV N-RNA rings (21), we identified 20 residues at the surface of N protomer that could be involved in the interaction with P40 (Fig. 2*B*). Among these residues, 18 residues are implicated in the interaction with the N-arm of N_{i+1} protomer, and the two residues Ile-270 and Tyr-353, are involved in the interaction with the C-arm of N_{i-1} protomer. We first attempted to determine the impact of alanine substitution of these residues on the polymerase activity using the minigenome assay, as described previously (22, 23). Preventing the formation of an N^0-P complex competent for genomic or antigenomic RNA encapsidation would result in a decrease in N-RNA template formation, and therefore of mRNA transcription and expression of the luciferase (Luc) reporter. Although no main impact on N expression was observed (Fig. 2*D*), alanine substitution of the 5 residues Leu-272, Met-281, Tyr-288, Phe-300, and Phe-320 totally abrogated polymerase activity, and 11 other mutants displayed a reduction of luciferase activity of about or more than 50% compared with WT N protein (Fig. 2*C*). Only 4 mutations (K81A, I82A, V262A, and Y353A) had no impact on the polymerase activity.

To further investigate the impact of these mutations, we then studied the cellular localization of N. As previously described, co-expression of N and P proteins leads to the formation of inclusion bodies (IBs) similar to the structures observed during RSV infection (24, 25) (Fig. 3) that were recently shown to be the sites of RSV replication and transcription (26). No impact on IB morphology was detected upon substitution of residues Lys-81, Ile-82, Val-262, Val-285, Gly-296, and Tyr-353 (not shown and Table 1). On the contrary, a total loss of IB formation was observed when mutating residues Lys-272, Met-281, Tyr-288, Phe-300, and Phe-320 (Fig. 3 and Table 1). More surprisingly, the absence of IBs was also observed in the presence of N substitutions M248A and L258A that respectively displayed 30 and 50% of polymerase activity (Table 1). Finally, a main defect on IB formation (decrease in number and size of IBs compared with the WT) was observed upon mutation of residues Val-224, His-225, Ile-228, Phe-247, Arg-259, Ile-270, and Val-284 (Fig. 3 and Table 1).

Taken together, these results show that, among the 20 targeted N residues, 16 are critical for N function within the polymerase complex. However, given the specific localization of targeted residues, the strong effect of mutations on polymerase activity and N localization could be attributed to either a major defect in (i) intrinsic N conformation, (ii) N–N interaction, or (iii) N–P40 interaction.

Identification of N residues involved in P40 binding

We then assessed the potential impact of N mutations on its structure and its capacity to interact with RNA. As previously described, co-expression in bacteria of N with GST-PCT, which corresponds to a fusion protein between the GST and the fragment P(161–241) that interacts with the N_{NTD}, allows purifying N-RNA rings using the GST tag (21, 23). Mutations were thus introduced in the pET-N vector, and the ability of N (WT or mutants) to co-purify with GST-PCT was evaluated by SDS-PAGE and Coomassie Blue staining (Fig. 4*A*). Among the 18 N variants tested, only 8 (V224A, M248A, L258A, V262A, V285A, G296A, I270A, and Y353A) were co-purified with GST-PCT with similar amounts compared with WT N. The mutations of the 5 residues His-225, Ile-228, Phe-247, Met-281, and Val-284 seemed to alter the interaction with PCT. Finally, the 5 mutants R259A, L272A, Y288A, F300A, and F320A were not pulled down by GST-PCT, suggesting a strong impact of these mutations on the structural integrity of N. These results correlate with those obtained for the functional minigenome assay and IB morphology (Table 1).

We then focused on the mutants that could still interact with GST-PCT and tried to decipher if the targeted residues could be involved in the interaction with either P40 or the N-arm of N. To this end, 11 mutations were introduced in pET-$N_{\Delta 30}$ vector. $N_{\Delta 30}$ protein (WT or mutant) was co-expressed in bacteria together with either GST-N30 (30 N-terminal residues of N) or GST-P40, and the ability of monomeric N to be pulled down was evaluated by SDS-PAGE and Coomassie Blue staining. As shown in Fig. 4*B*, the 5 mutations V224A, M248A, L258A, M281A, and V284A induced a loss of interaction between $N_{\Delta 30}$ and GST-N30. On the contrary, these mutations poorly affected the interaction with GST-P40, except for L258A and

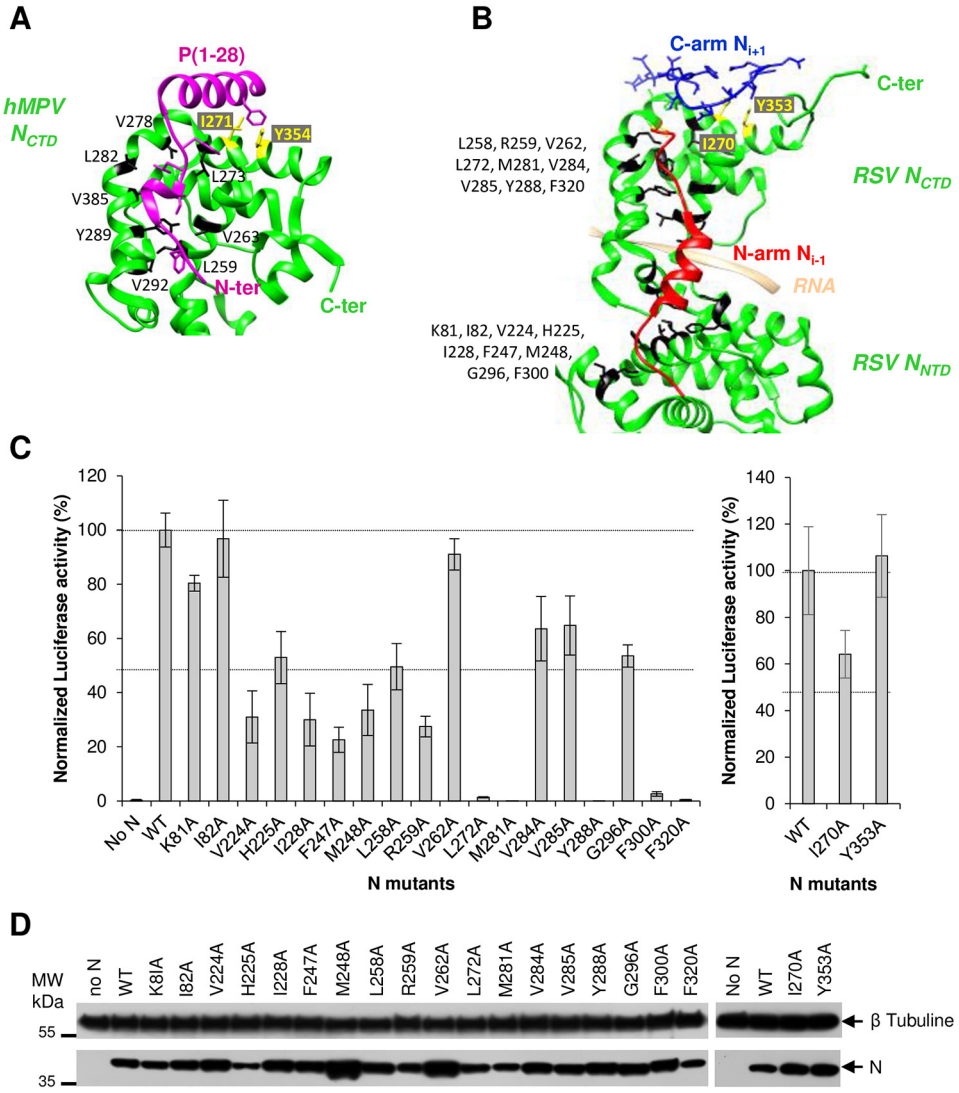

Figure 2. Search for the P40-binding site at the surface of N. *A*, ribbon representation of the hMPV N_{CTD} (*green*) in interaction with the peptide of P (residues 1–28, *purple*). The residues of N involved in the interaction with P are colored in *black* and *yellow* and the side chains are shown (PBD ID: 5FVD). *B*, ribbon representation of a part of RSV N protomer (*green*) from N-RNA 3D crystal structure (PBD ID: 2WJ8) showing binding of the N_{i-1} N-arm (in *red*) and of the N_{i+1} C-arm (in *blue*). Residues involved in N_{i-1} N-arm or in N_{i+1} C-arm binding, and that could also interact with P40, are colored in *black* and *yellow*, respectively, and their side chains are shown. *C*, effect of N mutations on RSV polymerase activity. BSRT7/5 cells were transfected with plasmids encoding the WT P, M2–1, and L proteins, the pMT/Luc minigenome, and WT or mutant N proteins, together with pCMV–β-gal for transfection standardization. Viral RNA synthesis was quantified by measuring the luciferase activity after cell lysis 24 h after transfection. Each luciferase minigenome activity value was normalized based on β-gal expression and is the average of three independent experiments performed in triplicate. *Error bars* represent standard deviations calculated based on three independent experiments made in triplicate. *D*, Western blotting showing the expression of N protein variants in BSRT7/5 cells.

V284A substitutions that seemed to interact less efficiently with GST-P40. More interestingly, the mutation I270A specifically abrogated the interaction with GST-P40 without affecting the interaction with GST-N30 (Fig. 4*B*). Finally, the Y353A substitution, which had no impact on minigenome activity or on N oligomerization, induced a defect of interaction of $N_{\Delta 30}$ with both GST-N30 and GST-P40. We thus cannot exclude a defect of $N_{\Delta 30}$ folding for this mutant protein.

Although our results suggest that most of the introduced mutations strongly affect N conformation, we clearly reveal the direct role of N residue Ile-270 in the interaction with P40. The data also suggest a role of N residues Leu-258 and Val-284 in the interaction. These results confirm the strong structural homology between RSV and hMPV N⁰-P complexes, with the P-binding domain on N⁰ overlapping both the N_{i-1} N-arm– and N_{i+1} C-arm–binding sites involved in N oligomerization (Fig. 2*A*).

Modeling the structure of RSV N⁰-P complex in solution

To gain information on the structure of the N⁰-P complex, small angle X-ray scattering (SAXS) and analytical ultracentrifugation (AUC) approaches were then combined to provide information about the overall size, shape, and stoichiometry of this complex in solution (Fig. 5). After purification of the $N_{\Delta 30}$-P40 complex, we first analyzed the complex by AUC (Fig. 5*A*). One main species with a sedimentation coefficient of 3.4 ± 0.15 *s* and a frictional ratio of 1.3 compatible with a complex form of one N⁰ and one peptide P40 was detected (Table 2). This single population suggests a really stable interaction between N⁰ and P peptide as previously measured (17). On the other hand, the

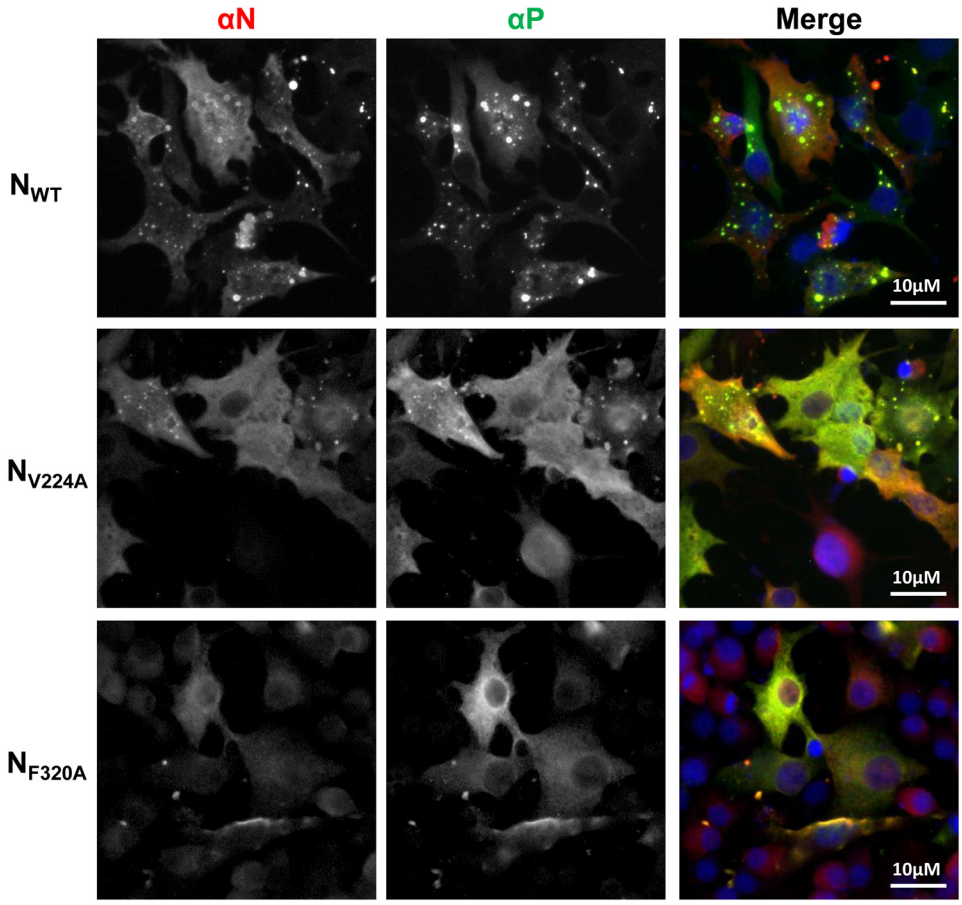

Figure 3. Impact of N mutations on the formation of cytoplasmic inclusion bodies. N and P proteins were coexpressed in BSRT7/5 cells; cells were then fixed 24 h post transfection and labeled with anti-P (*green*) and anti-N (*red*) antibodies, and the distribution of viral proteins was observed by fluorescence microscopy. Nuclei were stained with DAPI. *Scale bars*, 10 μm.

Table 1
Characterization of the mutants of N
ND, not determined.

N mutants	Polymerase activity (%)[a]	Inclusion bodies	Co-purification with		
			GST-PCT	GST-40	GST-N30
K81A	80	+	ND	ND	ND
I82A	95	+	ND	ND	ND
V224A	30	+/−	+	+	−
H225A	50	+/−	+/−	+	+
I228A	30	+/−	+/−	ND	ND
F247A	25	+/−	+/−	ND	ND
M248A	30	−	+	+	−
L258A	50	−	+	+/−	−
R259A	25	+/−	−	ND	ND
V262A	90	+	+	+	+
I270A	55	+/−	+	−	+
L272A	5	−	−	ND	ND
M281A	0	−	+/−	+	−
V284A	60	+/−	+/−	+/−	−
V285A	60	+	+	+	+
Y288A	0	−	−	ND	ND
G296A	50	+	+	+	+
F300A	5	−	−	ND	ND
F320A	0	−	−	ND	ND
Y353A	110	+	+	−	+/−

[a] Values corresponding to rounded-up averages.

molecular weights derived from Guinier analysis of the SAXS data reveal no sample aggregation or radiation damage. In agreement with AUC experiments (Table 2), we found that the $N_{\Delta 30}$-P40 complex behaves as a monodisperse distribution of monomers in one to one complex in solution. The estimated molecular mass of the complex derived from the extrapolated intensity I(0) at the origin is consistent with the theoretical value of 45.3 kDa (Table 2 and Table S1). The maximum distance (D_{max}) and the radius of gyration (R_g) of the $N_{\Delta 30}$-P40 complex derived from the electron pair distance distribution

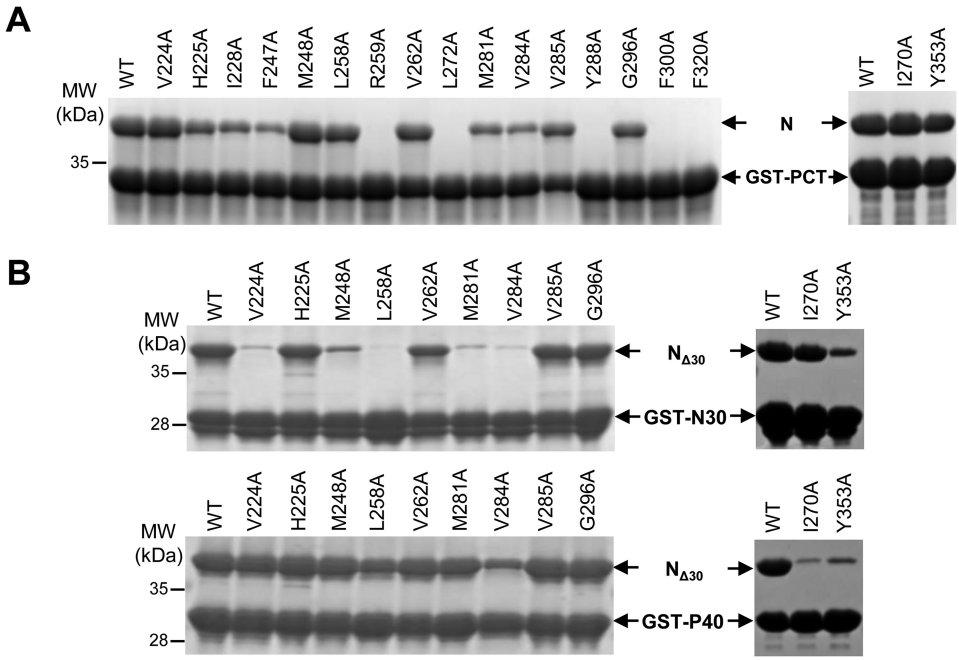

Figure 4. Impact of N mutations on N-P and N-N interactions. *A*, full-length N constructs (WT or mutants) were co-expressed with GST-PCT in *E. coli* and complexes were pulled down using GST tag. *B*, $N_{\Delta 30}$ constructs (WT or mutants) were co-expressed with GST-P40 or GST-N30 in *E. coli* and complexes were pulled down using GST tag. Co-purification of N (or $N_{\Delta 30}$) with GST constructs was analyzed by SDS-PAGE and stained with Coomassie Blue.

function $P(r)$ were respectively 9.41 nm and 2.74 nm (Table 2 and Fig. 5*B*). The normalized Kratky plot is characteristic of a multidomain protein with flexible regions (Fig. 5*C*). To gain further understanding of the structural arrangement of the complex, we used Coral to generate 50 structures of the $N_{\Delta 30}$-P40 complex, taking as starting configuration a model based on the X-ray structures of RSV N (PDB ID: 2WJ8) and hMPV N^0-P complex (PDB ID: 5FVD), with a random arrangement of the C-terminal end of P40. Briefly, during the modeling process, the P40 peptide and the globular domain (256–359) of N were fixed in position to maintain the contact between the N_{CTD} surface and the P40 peptide based on the crystal structure of the hMPV N^0-P complex. During the process, the last 13 amino acids in the C-terminal end of P40, the linker between the two globular domains of N, as well as the C-arm of N were in random conformation, generating a large amount of interdomain and C-arm orientations. The chi^2 value, deduced from the difference between the calculated SAXS curves of the models and the experimental data, as well as the calculated theoretical sedimentation values were used to select the best models that were representative of the SAXS curve. Of the 50 models generated by Coral, only 18 were compatible with the AUC data.

Of these 18, the best 5 models that were in agreement with both the experimental SAXS data and the AUC hydrodynamic parameters are presented here (Fig. 5*E*). Interestingly, these selected conformers display two main possible orientations of the C-arm of N depending on the relative position of the N_{CTD} and N_{NTD} domains. In one case (two superimposed models in Fig. 5*E, left*), the RNA groove access is blocked by the positioning of the N C-arm in the groove and the N_{CTD} and N_{NTD} domains are maintained in an open conformation. In the second case (three superimposed models in Fig. 5*F, right*), the N_{CTD} and N_{NTD} domains are maintained in a close conformation and N C-arm is flexible. However, the best model presented in Fig. 5, *D* and *F* suggests that the RNA groove access is blocked by the positioning of the N C-arm in the groove as already described for hMPV (16). In conclusion, our models support the strong structural similarity between the N^0-P complexes of RSV and hMPV, and suggest a high flexibility of the N C-arm.

Mutations in the N C-arm strongly affect the RNA polymerase activity

Based on our results and hMPV structure, we hypothesized that the C-arm of N is a flexible region that impairs interaction between the neosynthesized N^0 nucleoprotein and RNA by blocking the access of the RNA-binding groove of N. Hence, in addition to the chaperone role of P, the C-arm of N would also contribute to the transition from the N^0-P to the N-RNA bound complexes. It is noteworthy that the N C termini of RSV and other pneumoviruses are characterized by the presence of conserved acidic and hydrophobic amino acid residues (Fig. 6*A*). Such residues could play a major role by interacting with the positively charged N RNA-groove. We thus investigated the role of these N residues on the activity of the polymerase complex by site-directed mutagenesis using the RSV minigenome assay. The C-terminal acidic (Glu-373, Glu-376, Asp-386, Asp-388, Glu-373+Glu-374, Asp-386+Asp-388) and hydrophobic (Leu-368, Leu-370, and Leu-382) residues of N were substituted by alanine, and the functionality of these N variants within the polymerase complex was assayed. Similarly, the potential phosphorylated residues Ser-366 and Thr-371 were substituted by either alanine or aspartic acid. As shown in Fig. 6*B*, no major effect on the RNA polymerase activity was observed for S366A, S366D, and L382A variants. However, the E373A, E376A, D386A, D386A/D388A, T371A, and T371D substitutions

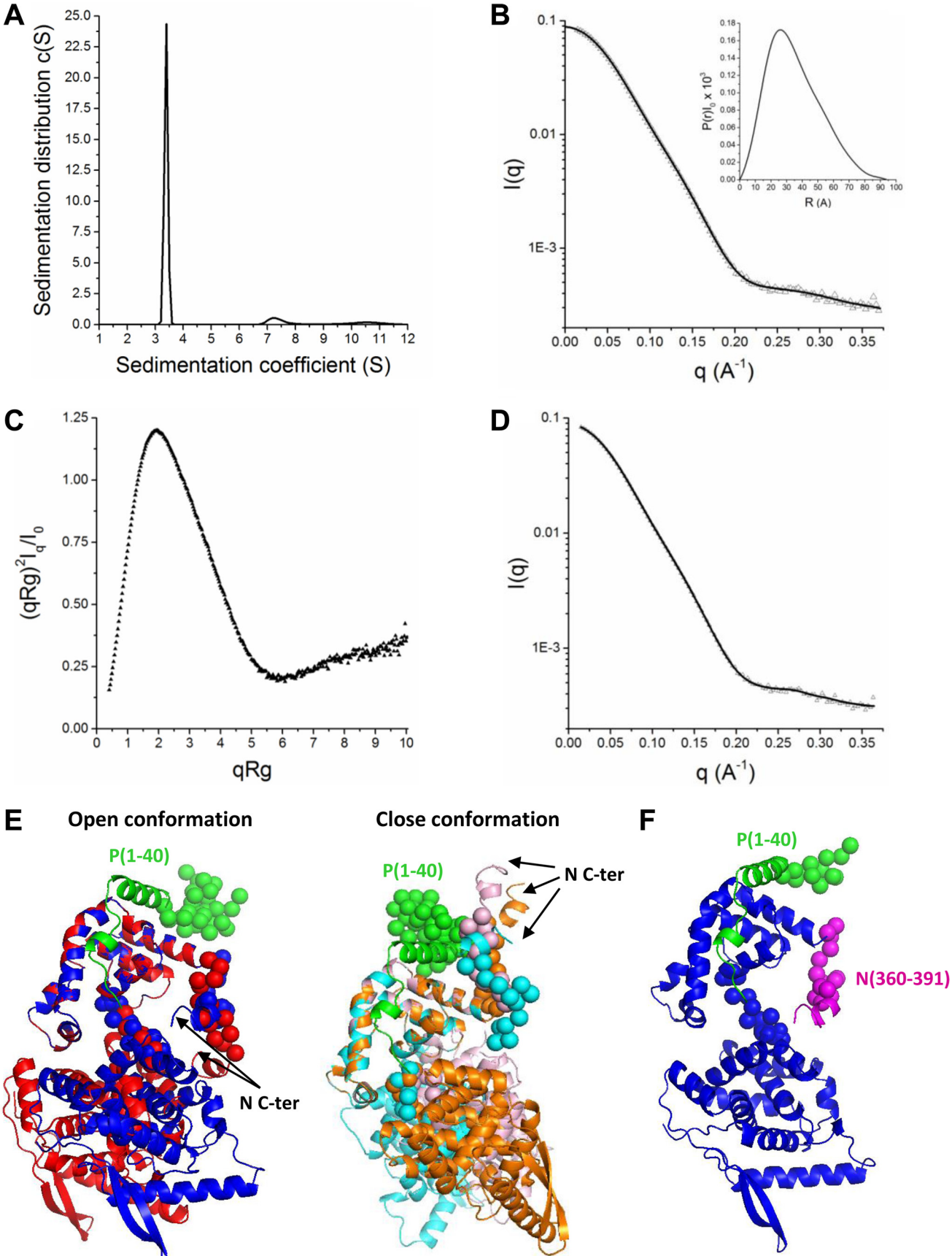
A
Sedimentation distribution c(S)
Sedimentation coefficient (S)
B
I(q)
q (A-1)
P(r)I0 x 10-3
R (A)
C
(qRg)2Iq/I0
qRg
D
I(q)
q (A-1)
E
Open conformation
Close conformation
P(1-40)
P(1-40)
N C-ter
N C-ter
F
P(1-40)
N(360-391)

Table 2

Summary of hydrodynamic and structural parameters and comparison with theoretical values calculated for all 3D models

Experimental values were measured by SAXS, AUC. Models were generated by Coral and chi² value of the model were calculated by comparison to the experimental SAXS curve. R_g, D_{max}, and S theoretical values were determined with HydroPro for all 3D models with and average size for each amino acid of 4.84 Å to take in consideration the hydration layer.

	R_g [Å]	D_{max} [Å]	Chi²	S [S]	f/f₀
Experimental value					
$N_{\Delta30}$-P40 complex	27.4	94.1	ND	3.4 ± 0.15	1.3
Coral models Calculated values					
Model 1	27.6	107.5	1.56	3.26	1.35
Model 2	27.0	103.6	1.63	3.30	1.34
Model 3	27.4	108.0	1.64	3.26	1.35
Model 4	27.3	101.9	1.65	3.28	1.35
Model 5	27.1	103.0	1.68	3.26	1.35

resulted in an approximatively 50% reduction of luciferase activity compared with WT N. Finally, the E373A/E374A, L368A, and L370A substitutions had the strongest effect, with a reduction of more than 90% of the polymerase activity. It is noteworthy that all N mutants were shown to be expressed in similar amounts in BSRT7 cells compared with WT N protein (Fig. 6*C*). Altogether, these results show that conserved acidic and hydrophobic residues of the C-arm of N play a major role in the function of N within the polymerase complex.

The N C-arm is directly involved in the inhibition of RNA binding

To determine whether the decrease in the polymerase activity observed with the N C-arm Ala mutants was correlated to a defect of N⁰-P complex conformation, the same mutations were introduced in the plasmid expressing $N_{\Delta30}$ in *E. coli*, to generate 11 N variants. GST-P40 was coexpressed with the WT or mutant forms of $N_{\Delta30}$ in *E. coli* and purified on GSH-Sepharose beads. The resulting purified GST-P40-$N_{\Delta30}$ complexes were analyzed by SDS-PAGE. Only the E373A/E374A mutant could not be purified, suggesting that this double mutation has a dramatic impact on the P40-$N_{\Delta30}$ complex formation (Fig. 7*A*). All of the 10 other N mutant proteins were efficiently purified using GST-P40, showing that these mutations did not affect the P-N interaction. Next, the GST tag was cleaved by TEV protease and the $A_{260\,nm}/A_{280\,nm}$ ratio of isolated $N_{\Delta30}$-P40 complexes was measured and compared with either N-RNA rings or $N_{\Delta30}$ alone (purified with a C-terminal His tag). As shown in Table 3, the $A_{260\,nm}/A_{280\,nm}$ ratios of $N_{\Delta30}$ purified alone or in the presence of P40 were 0.87 and 0.63, respectively, confirming that P40 is required to efficiently block the interaction of N with RNA. Although all the $N_{\Delta30}$-P40 complexes displayed an $A_{260\,nm}/A_{280\,nm}$ ratio <1 and close to 0.6 like WT $N_{\Delta30}$, a slight increase of this ratio was detected for most of the mutants, especially for mutants L368A, and L370A (Table 3), suggesting the presence of some amounts of RNA associated to these complexes.

Given that N-RNA and N⁰-P forms of N present similar secondary structure as revealed by CD spectra (Fig. 1*D*), it is likely that binding of the N C-arm into the RNA-binding groove induces only minor conformational changes. To investigate the impact of mutations in the N C-arm on N folding, we took advantage of the presence of a single tryptophan residue (Trp-260) in N, located close to the N RNA-binding groove (Fig. 7*B*), because λ_{max} of emission of a tryptophan reflects the polarity of its environment. In a hydrophilic environment, λ_{max} shifts to 400 nm and the intensity, although in an apolar environment, λ_{max} shifts to 300 nm. To validate that the fluorescence of Trp-260 could be used to characterize the local structural change of N close to the RNA-binding groove, we first measured the Trp λ_{max} of N-RNA rings and of $N_{\Delta30}$ purified alone or in the presence of P40. As shown in Table 3, the λ_{max} values of these proteins are 327 nm, 339 nm, and 330 nm, respectively. When interacting with RNA, the Trp-260 residue of N is in an apolar environment. The slight difference of λ_{max} value and intensity detected between N-RNA and $N_{\Delta30}$-P40 suggests that Trp-260 is maintained in a constrained environment within the N⁰-P complex. This hypothesis is supported by the important shift of λ_{max} value measured for the $N_{\Delta30}$ alone that clearly revealed the polar environment of the Trp. The strong difference between the λ_{max} values measured for $N_{\Delta30}$-P40 and $N_{\Delta30}$ alone could be attributed to (i) the binding of P40 on N and/or (ii) the interaction of the N C-arm close to the RNA groove. We then investigated the impact of mutations in the N C-arm on the λ_{max} of purified recombinant $N_{\Delta30}$-P40 complex. Although no major change in the λ_{max} values was detected for most of the mutants, a slight change in the fluorescence spectra was detected when mutating residues Ser-266 or Thr-271, and a strong switch of the Trp λ_{max} values, up to 337 nm, was detected for mutants L368A and L370A (Table 3). We consider that these changes were significant as they correspond to tendencies over many data points obtained for two independent protein purifications. These variations in Trp fluorescence reveal that Trp-260 is more exposed to the solvent when mutating the residues Leu-368 and Leu-370. Altogether, these data indicate that the residues Leu-368 and Leu-370 are critical for stabilization of the N⁰-P complex, and could be directly involved in the interaction of the C-arm close to the N-RNA– binding groove, confirming our initial hypothesis.

Discussion

The viral RNA genome and anti-genome of *Mononegavirales* are coated by the viral N protein at all times. Efficient replication of genomic and antigenomic RNAs depends on the neo-

Figure 5. Structural characterization of RSV $N_{\Delta30}$-P40 in solution. *A*, analytical ultracentrifugation sedimentation distribution analysis of RSV $N_{\Delta30}$-P40. *B*, scattering curve of RSV $N_{\Delta30}$-P40 complex (*triangle*) with fitted curve (*plain line*) used to generate distance distribution. *Inset*, distance distribution functions obtained using the program GNOM. *C*, dimensionless Kratky plot. *D*, fit of the best Coral model (see *F*). *E*, presentation of the five best Coral models of RSV $N_{\Delta30}$-P40 complex superimposed based on the two main possible orientations of the C-arm of N and on the relative position of the N_{CTD} and N_{NTD} domains. *Left*, the RNA groove access is blocked by the positioning of the N C-arm in the groove and the N_{CTD} and N_{NTD} domains are maintained in an open conformation. *Right*, the N_{CTD} and N_{NTD} domains are maintained in a close conformation and N C-arm is flexible. The P40 peptide is represented in *green* and the C terminus of N is indicated. *F*, ribbon representation of the best structural Coral model of RSV $N_{\Delta30}$-P40 complex. The N protomer (residues 31–382) is represented in *blue*, the C-arm of N (residues 383–391) in *purple*, and the P40 peptide in *green*. Linker regions are represented by *spheres*.

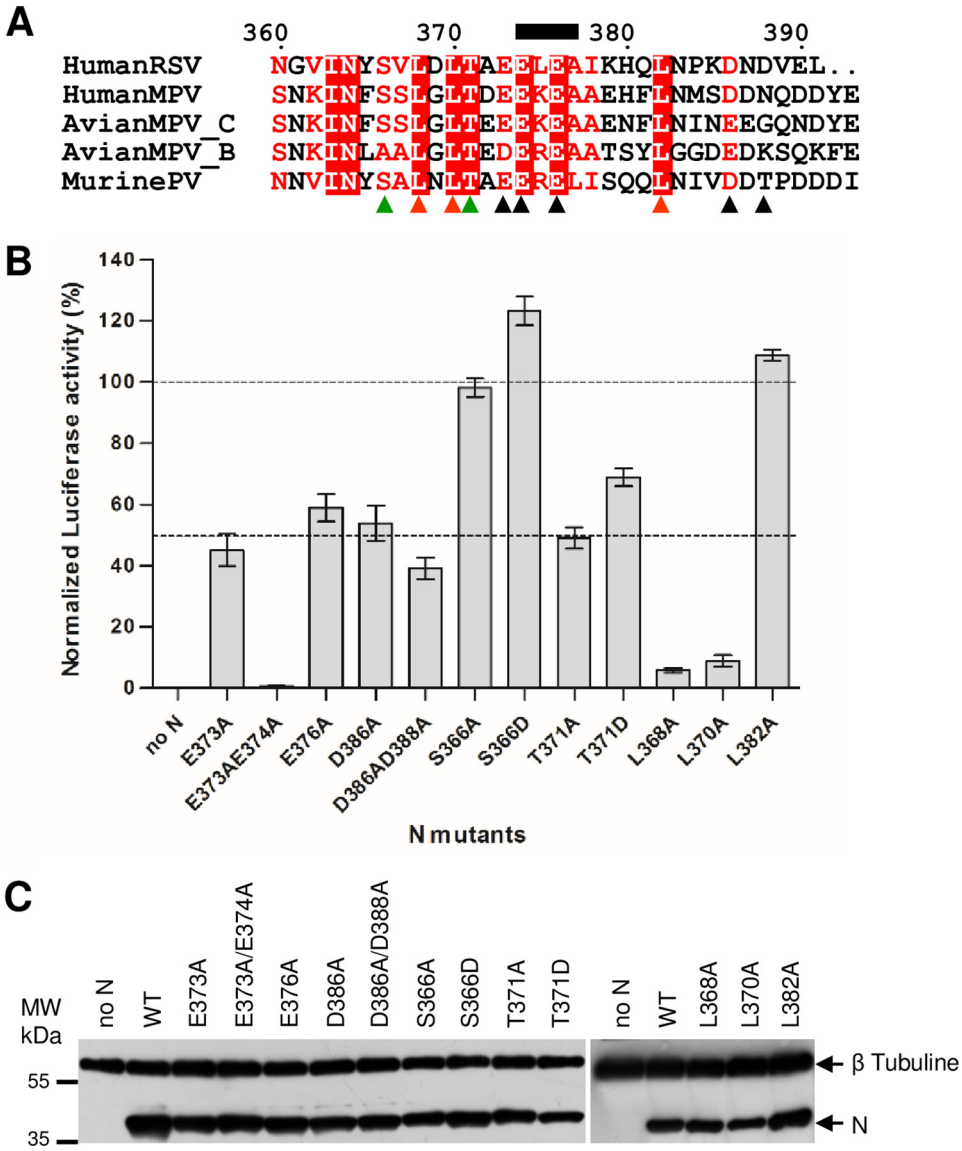

Figure 6. Effect of mutations in the C-arm of N on the RSV polymerase activity. *A*, sequence alignments of the C-arms of N proteins from viruses belonging to the *Pneumoviridae* family. UniProt accession codes: NCAP_HRSVA (human RSV); A1DZS3_9MONO (human MPV), A4KZ90_9MONO (avian MPV_C); A7DV59_9MONO (avian MPV_B), NCAP_MPV15 (murine pneumonia virus). Invariant residues are highlighted in *white font* on a *red* background. The short α-helix observed in the crystal structure of N (21) is indicated above the sequence by a *black rectangle*. *Triangles* under the alignment mark mutated residues: acidic (*black*), hydrophobic (*red*), and Ser/Thr (*green*). *B*, RSV polymerase activity in the presence of N mutants. BSRT7/5 cells were transfected with plasmids encoding the WT P, M2–1, and L proteins; the pMT/Luc minigenome; and WT or mutant N proteins, together with pCMV–β-gal for transfection standardization. Viral RNA synthesis was quantified by measuring the luciferase activity after cell lysis 24 h after transfection. Each luciferase minigenome activity value was normalized based on β-gal expression and is the average of three independent experiments performed in triplicate. *Error bars* represent standard deviations calculated based on three independent experiments made in triplicate. *C*, Western blotting showing the expression of N protein variants in BSRT7/5 cells.

synthesis of the N protein that has to be maintained monomeric and RNA-free (N^0) to specifically encapsidate these replication products as they are synthesized. It is noteworthy that all these N proteins present a strong propensity to oligomerize and to bind to RNA, and that these two mechanisms are concomitant. As a consequence, both mechanisms have to be impaired at the same time to maintain a pool of N competent for RNA encapsidation. For this, viruses of the *Mononegavirales* order share a common strategy, which depends on the chaperone activity of the P N-terminal region that binds to N, forming a N^0-P complex (5). It is noteworthy that the N proteins of *Mononegavirales* present a similar architecture and are composed of two globular domains (N_{NTD} and N_{CTD}) linked by a hinge region that forms the RNA groove, and N- and C-arms that are involved in N oligomerization. However, besides strong similarities between N^0-P complexes, the mechanisms involved in the inhibition of RNA binding to N differ (10–15).

Here, by deleting the N- and C-arms of RSV N, we observed that both the presence of the peptide P(1–40) and the deletion of the N-arm of N ($N_{\Delta 30}$) are required to purify a stable monomeric N protein from *E. coli*. We also noticed that the C-arm of N is directly involved in the inhibition of the interaction of N with RNA (Fig. 1). Based on the crystal structures of RSV N-RNA and hMPV N^0-P complexes, we then tried to characterize the surface of N involved in P40 binding. We identified some residues potentially involved in P40 binding, generated N

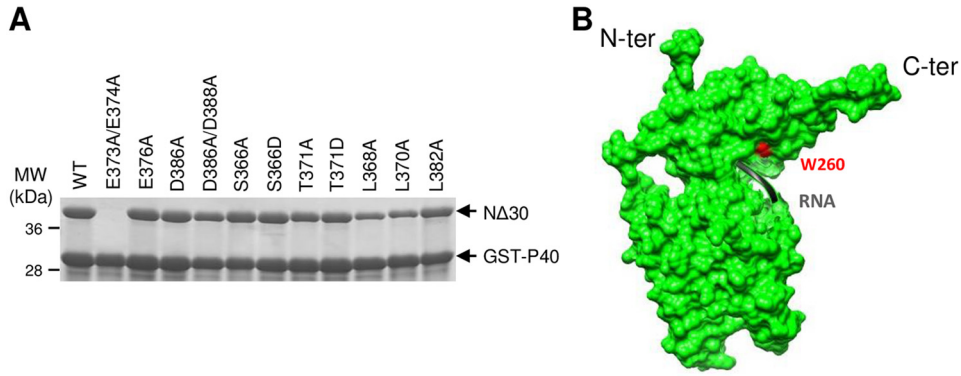

Figure 7. Purification of C-arm mutants of N from *E. coli*. *A*, $N_{\Delta 30}$ constructs (WT or mutants) were co-expressed with GST-P40 in *E. coli* and complexes were pulled down using GST tag. Co-purification of WT and mutants of $N_{\Delta 30}$ with GST-P40 was analyzed by SDS-PAGE and Coomassie Blue staining. *B*, surface view of an RSV N monomer showing the position of RNA and of the Trp-260 residue. N and C termini of N are indicated.

Table 3
Characterization of the recombinant N proteins

	Protein	OD_{260nm}/OD_{280nm}	Trp fluorescence* λ_{max} value (nm)
	N-RNA	1.36	327
	$N_{\Delta 30}$	0.87	339
	$N_{\Delta 30}$+P40	0.62	330
$N_{\Delta 30}$ mutants+P40	**E376A**	0.64	330
	D386A	0.63	330
	D386A/D388A	0.67	330
	S366A	0.70	331
	S366D	0.64	332
	T371A	0.69	332
	T371D	0.68	333
	L368A	0.95	337
	L370A	0.88	336
	L382A	0.63	330

[a] For concentration of protein of 10 μM λex 295 nm.

mutants, and used both cellular and biochemical assays to validate the role of these residues. Although most of the mutations resulted in impaired N purification, we identified the residue Ile-270 as directly and specifically involved in the interaction with P40. Our results also revealed a role of N residues Leu-258 and Val-284 in the P40-N interaction.

Structural information on the RSV $N_{\Delta 30}$-P40 complex in solution was then obtained by combining SAXS and AUC approaches. Models were generated by fixing in position the P40 peptide at the N_{CTD} surface based on the crystal structure of the hMPV N⁰-P complex (16). These models show that monomeric N easily accommodates the structure of an N protomer from the N-RNA ring 3D structure, with a high flexibility of the N C-arm and of the linker region between N_{CTD} and N_{NTD} (Fig. 5*E*). Although some models suggest that N_{CTD} and N_{NTD} domains could be maintained in a close conformation with the N C-arm flexible, the best model suggests that the N C-arm could bind close to the RNA groove to impair its accessibility (Fig. 5*F*), as described for the N⁰-P complex of hMPV. To confirm these results, we generated N mutants of the N C-arm and showed that the acidic and hydrophobic residues of the C-arm of N are critical for its activity. More specifically, residues Leu-368 and Leu-370 of N were shown to be directly involved in the inhibition of RNA binding. These results correlate with the observation of Renner *et al.* (16) reporting semi-conserved LGLT-motif within the CTD-arms of the N proteins of *Paramyxoviridae* which is followed by a stretch of residues with helical propensity. It is noteworthy that the C-arms of N proteins of the *Pneumoviridae* family are composed of conserved acidic and hydrophobic residues. Such acidic and hydrophobic motifs are reminiscent of eukaryotic acidic activation domains, in which acidic residues are used to promote long-range electrostatic interactions to attract their basic targets, and then undergo an induced structural transition to an α-helix to enable the contact with the target through hydrophobic residues (27).

In conclusion, our results point out the strong structural homology between RSV and hMPV N⁰-P complexes. These viruses present an original mechanism among *Mononegavirales* to impair RNA binding that involves (i) a specific interaction of the C-arm of N with the RNA groove and (ii) the binding surface of P peptide that overlaps with both interaction sites of neighboring N protomers within N-RNA rings (*i.e.* of N_{i+1} C-arm and N_{i-1} N-arm). It is noteworthy that the crystal structure of the monomeric nucleoprotein of influenza virus that belongs to *Orthomyxoviruses* and which does not present homolog of the P protein, also revealed that the C terminus of the nucleoprotein monomer is bound to the side of the RNA-binding surface (28). This binding allows reducing the positive charge of the RNA groove to impair RNA binding. These observations thus suggest that the members of the negative-strand viruses present conserved mechanisms to control the specificity of viral genome encapsidation. Although the 3D structure of the RSV N⁰-P still remains to be solved, these structural data pave the way to the rational design of specific protein–protein interaction inhibitors for these viruses that represent main respiratory pathogens because compounds that stabilize or destabilize the monomer may slow down viral infection. We and

others already proposed that inhibitory peptides mimicking the P peptide could represent potent new antivirals not only against RSV but also for other *Mononegavirales* (11, 17, 29). Such approaches were developed to interfere with the fusion step of RSV, using stapled peptides (30, 31). Finally, these structural data revealed that the surface of interaction between the N C-arm and the RNA groove could constitute a second target to develop antivirals against the N^0-P complex. In this case, stabilization of the interaction using small molecules could represent an attractive strategy (32).

Experimental procedures

Plasmid constructions

All the viral sequences were derived from the hRSV strain Long, ATCC VR-26 (GenBank™ accession no. AY911262.1). N- and/or C-terminal N deletions were made by PCR using *Pfu* DNA polymerase (Stratagene). PCR products were cloned in the pET28a+ vector to produce truncated N proteins either with no tag or with a C-terminal His_6 tag. The pGEX-N30 plasmid coding for the 30 N-terminal residues of N fused to GST was obtained by cloning annealed oligonucleotides at BamHI restriction site of the pGEX4T3 vector. The pGEX-PCT and pGEX-P40 vectors coding respectively for P(161–241) and P(1–40) in fusion with GST were described previously (17). Point mutations were introduced in pET-N by site-directed mutagenesis, using the QuikChange Site-Directed Mutagenesis Kit (Stratagene). Sequence analysis was carried out to check the integrity of all the constructs.

Plasmids for eukaryotic expression of the hRSV N, P, M2–1, and L proteins designated pN, pP, pM2–1, and pL, have been described previously (33, 34). The pM/Luc subgenomic minigenome which encodes the firefly luciferase (Luc) reporter gene under the control of the M/SH gene start sequence was derived from the pM/SH subgenomic replicon (35) and has been described previously (22). Point mutations were introduced in pN by site-directed mutagenesis as described above.

Antibodies

The following primary antibodies were used for immunofluorescence and/or immunoblotting: a mouse monoclonal anti-N protein (Serotec, Oxford, UK), rabbit anti-P and rabbit anti-N antisera (23, 34), and a mouse monoclonal anti–β-tubulin (Sigma-Aldrich). Secondary antibodies directed against mouse and rabbit IgG coupled to HRP were used for immunoblotting (P.A.R.I.S., Compiègne, France), and goat anti-rabbit and anti-mouse antibodies coupled to Alexa Fluor 448 and Alexa Fluor 594 were used for immunofluorescence.

Cell culture and transfections

BHK-21 cells (clone BSRT7/5) constitutively expressing the T7 RNA polymerase (36) were grown in Dulbecco's modified Eagle's medium (Lonza, Cologne, Germany) supplemented with 10% fetal calf serum (FCS), 2 mM glutamine, and antibiotics. Cells were transfected using Lipofectamine 2000 (Invitrogen) as described by the manufacturer.

Minigenome assay

Cells at 90% confluence in 48-well dishes were transfected with a plasmid mixture containing 125 ng of pM/Luc, 125 ng of pN, 125 ng of pP, 62.5 ng of pL, and 31 ng of pM2–1 as well as 31 ng of pRSV–β-gal (Promega) to normalize transfection efficiencies (22). Transfections were done in triplicate, and each independent transfection was performed three times. Cells were harvested 24 h post transfection, then lysed in luciferase lysis buffer (30 mM Tris, pH 7.9, 10 mM $MgCl_2$, 1 mM DTT, 1% Triton X-100, and 15% glycerol). The luciferase activities were determined for each cell lysate with an Infinite 200 Pro (Tecan, Männedorf, Switzerland) and normalized based on β-gal expression.

Fluorescence microscopy

Immunofluorescence microscopy was performed with cells grown on coverslips and previously transfected with pN and pP. At 24 h post transfection, cells were fixed with 4% paraformaldehyde for 30 min. Fixed cells were made permeable and blocked for 15 min with PBS containing 0.1% Triton X-100, 3% bovine serum albumin (BSA). Cells were then successively incubated for 1 h at room temperature with primary and secondary antibody mixtures diluted in PBS containing 3% BSA, 0.05% Tween. Coverslips were mounted with ProLong Gold Antifade reagent containing DAPI (Invitrogen), and observed with a Nikon TE200 microscope equipped with a CoolSNAP ES2 camera (Photometrics, Tucson, AZ). Images were processed by using Meta-Vue (Molecular Devices, San Jose, CA) and ImageJ software.

Expression and purification of recombinant proteins

E. coli BL21 bacteria (DE3) (Novagen, Madison, WI) transformed with pET-N– derived plasmids alone, or together with pGEX-PCT, pGEX-P40, or pGEX-N30 plasmids were grown at 37 °C for 8 h in 100 ml of Luria Bertani (LB) containing kanamycin (50 μg/ml) or ampicillin and kanamycin, respectively. The same volume of LB was then added and protein expression was induced by adding 80 μg/ml isopropyl-β-D-thio-galactoside to the medium. Bacteria were incubated for 15 h at 28 °C and then harvested by centrifugation. For the purification of the recombinant GST fusion proteins, bacterial pellets were re-suspended in lysis buffer (50 mM Tris-HCl, pH 7.8, 60 mM NaCl, 1 mM EDTA, 2 mM DTT, 0.2% Triton X-100, 1 mg/ml lysozyme) supplemented with cOmplete Protease Inhibitor mixture (Roche), incubated for 1 h on ice, sonicated, and centrifuged at 4 °C for 30 min at 10,000 × *g*. GSH-Sepharose 4B beads (GE Healthcare) were added to clarified supernatants and incubated at 4 °C for 3 h. Beads were then washed two times in lysis buffer and three times in PBS 1×, and stored at 4 °C in an equal volume of PBS. To isolate GST-free P40-$N_{\Delta 30}$ complex, beads containing bound complex were incubated with TEV protease for 16 h at 20 °C. For $N_{\Delta 30}$-His_6 fusion protein purification, bacterial pellets were re-suspended in lysis buffer (20 mM Tris-HCl, pH 8, 500 mM NaCl, 0.1% Triton X-100, 10 mM imidazole, 1 mg/ml lysozyme) supplemented with cOmplete Protease Inhibitor mixture (Roche). After sonication and centrifugation, lysates were incubated 30 min with chelating Sepharose Fast Flow beads charged with Ni^{2+} (GE Healthcare). Finally, beads

were successively washed in the washing buffer (20 mM Tris-HCl, pH 8, 500 mM NaCl) containing increasing concentration of imidazole (25, 50, and 100 mM), and proteins were eluted in the same buffer with 500 mM imidazole. Purified recombinant proteins were loaded onto a Sephacryl S-200 HR 16/30 column (GE Healthcare), eluted in 20 mM Tris-HCl, pH 8.5, 150 mM NaCl and characterized. The presence of RNA was determined by measuring the $A_{260\ nm}/A_{280\ nm}$ absorption ratio.

Circular dichroism spectroscopy

CD experiments were performed on a J-810 spectropolarimeter (Jasco, Tokyo, Japan) in a thermostated cell holder at 20 °C. Purified recombinant N proteins were dialyzed against 5 mM phosphate, 100 mM NaF, pH 8.5. Far-UV spectra (180–260 nm) were recorded using a bandwidth of 1 nm and an integration time of 1s, in a 0.5 mm path-length quartz cell with proteins at concentrations of 20 μM. Each spectrum was the average of 6 scans, with a scan rate of 100 nm/min. The spectra were corrected by subtracting the signal from the buffer, smoothed using the FFT filter (Jasco Software, Tokyo, Japan), and were treated as described previously (37).

Fluorescence spectroscopy

Fluorescence measurements were performed with an FP-750 spectrofluorimeter (Jasco, Tokyo, Japan) at 20 °C, using a 1-cm path length quartz cell, with proteins at a concentration of 10 μM. The excitation wavelength was fixed at 295 nm, and emission spectra were recorded from 300 to 360 nm at a scan rate of 125 nm·min^{-1}. The maximum emission wavelength (λ_{max}) represents the average of three values obtained from emission spectra. The measurements were performed on two independent purifications of each recombinant protein.

Analytical ultracentrifugation

Sedimentation velocity experiments were carried out at 20 °C in a ProteomeLab XL-I Analytical Ultracentrifuge (Beckman Coulter, Brea, CA) equipped with double-UV and Rayleigh interference detection. The purified protein-peptide complexes (1.1 mg/ml) were centrifuged at 42,000 rpm using an AN60-Ti rotor and 12-mm-thick Epon double sector centerpieces. Absorbance and interference profiles were recorded every 5 min. Buffer viscosity (η = 1.021 cP) and density (ρ = 1.0050° g.ml^{-1}) at 20 °C were estimated with SEDNTERP 1.09. Partial specific volumes at 20 °C were estimated based on amino acid sequences using SEDNTERP 1.09 software. Data were analyzed with SEDFIT 15.3 using a continuous size distribution c(S) model. Theoretical sedimentations of the complex were generated using HydroPro 10 (38).

Small angle X-ray scattering experiments

SAXS data were collected on the SWING beamline at Synchrotron SOLEIL (France) using the online HPLC system. SAXS samples were prepared in buffer (Tris 20 mM, pH 8, NaCl 150 mM, glycerol 5%). Protein complexes of $N_{\Delta 30}$-P40 complexes (50 μl) at 6 mg.ml^{-1} were injected into a size exclusion column (Bio SEC-3 300 Agilent column) cooled at 25 °C and eluted directly into the SAXS flow-through capillary cell at a flow rate of 200 μl·min^{-1}. The data were analyzed using FOXTROT and PRIMUS from ATSAS 2.7 (39), from which Guinier was generated. Scattering curves were selected for stable radius of gyration (R_g) at the apex of the elution profile, and the selected curves were averaged and buffer signal was subtracted. From these corrected scattering curves, the pair distribution function was computed using GNOM (40) and the normalized Kratky plot was generated (41). Furthermore, 50 low-resolution models, obtained from independent reconstructions, were generated using Coral (42) and a starting model of $N_{\Delta 30}$-P40 complex based on the X-ray structure of a N protomer derived from the N-RNA rings structure (PDB ID: 2WJ8) (21). The starting structure of N promoter was defined from N-terminal end as a succession of three folded domains (30–249; 256–359; 374–382) connected through two linker regions between the first two domains and the last two domains. The P40 peptide was positioned on the N_{CTD} (residues 256–359) based on X-ray structure of hMPV N^0-P complex (16) with the C-terminal end of P40 defined as a flexible region of 13 amino acids.

Molecular graphics images were produced using Chimera and PyMOL software programs.

Author contributions—C. E., B. R., P. R., S. B., C.-A. R., J. F., and M. G. data curation; C. E., B. R., P. R., S. B., and M. G. formal analysis; B. R. and M. G. writing-original draft; J.-F. E. and M. G. supervision; J.-F. E. funding acquisition; J.-F. E. and M. G. writing-review and editing; M. G. conceptualization.

Acknowledgments—We thank the staffs of the synchrotron facilities SOLEIL for technical help with the beamlines SWING. We warmly thank Origène Nyanguile and Christina Sizun for skillful discussions and critical review of the manuscript.

References

1. Collins, P. L., and Melero, J. A. (2011) Progress in understanding and controlling respiratory syncytial virus: Still crazy after all these years. *Virus Res.* **162,** 80–99 CrossRef Medline
2. Afonso, C. L., Amarasinghe, G. K., Banyai, K., Bao, Y., Basler, C. F., Bavari, S., Bejerman, N., Blasdell, K. R., Briand, F. X., Briese, T., Bukreyev, A., Calisher, C. H., Chandran, K., Cheng, J., Clawson, A. N., *et al.* (2016) Taxonomy of the order Mononegavirales: Update 2016. *Arch. Virol.* **161,** 2351–2360 CrossRef Medline
3. Bakker, S. E., Duquerroy, S., Galloux, M., Loney, C., Conner, E., Eléouët, J. F., Rey, F. A., and Bhella, D. (2013) The respiratory syncytial virus nucleoprotein-RNA complex forms a left-handed helical nucleocapsid. *J. Gen. Virol.* **94,** 1734–1738 CrossRef Medline
4. Liljeroos, L., Krzyzaniak, M. A., Helenius, A., and Butcher, S. J. (2013) Architecture of respiratory syncytial virus revealed by electron cryotomography. *Proc. Natl. Acad. Sci. U.S.A.* **110,** 11133–11138 CrossRef Medline
5. Jamin, M., and Yabukarski, F. (2017) Nonsegmented negative-sense RNA viruses-structural data bring new insights into nucleocapsid assembly. *Adv. Virus Res.* **97,** 143–185 CrossRef Medline
6. Cowton, V. M., McGivern, D. R., and Fearns, R. (2006) Unravelling the complexities of respiratory syncytial virus RNA synthesis. *J. Gen. Virol.* **87,** 1805–1821 CrossRef Medline
7. Morin, B., Kranzusch, P. J., Rahmeh, A. A., and Whelan, S. P. (2013) The polymerase of negative-stranded RNA viruses. *Curr. Opin. Virol.* **3,** 103–110 CrossRef Medline
8. Ruigrok, R. W., Crépin, T., and Kolakofsky, D. (2011) Nucleoproteins and nucleocapsids of negative-strand RNA viruses. *Curr. Opin. Microbiol.* **14,** 504–510 CrossRef Medline

9. Karlin, D., and Belshaw, R. (2012) Detecting remote sequence homology in disordered proteins: Discovery of conserved motifs in the N-termini of Mononegavirales phosphoproteins. *PLoS One* **7,** e31719 CrossRef Medline
10. Leyrat, C., Yabukarski, F., Tarbouriech, N., Ribeiro, E. A., Jr., Jensen, M. R., Blackledge, M., Ruigrok, R. W., and Jamin, M. (2011) Structure of the vesicular stomatitis virus N^0-P complex. *PLoS Pathog.* **7,** e1002248 CrossRef Medline
11. Yabukarski, F., Lawrence, P., Tarbouriech, N., Bourhis, J. M., Delaforge, E., Jensen, M. R., Ruigrok, R. W., Blackledge, M., Volchkov, V., and Jamin, M. (2014) Structure of Nipah virus unassembled nucleoprotein in complex with its viral chaperone. *Nat. Struct. Mol. Biol.* **21,** 754–759 CrossRef Medline
12. Guryanov, S. G., Liljeroos, L., Kasaragod, P., Kajander, T., and Butcher, S. J. (2015) Crystal structure of the measles virus nucleoprotein core in complex with an N-terminal region of phosphoprotein. *J. Virol.* **90,** 2849–2857 CrossRef Medline
13. Kirchdoerfer, R. N., Abelson, D. M., Li, S., Wood, M. R., and Saphire, E. O. (2015) Assembly of the Ebola Virus Nucleoprotein from a Chaperoned VP35 Complex. *Cell Rep.* **12,** 140–149 CrossRef Medline
14. Zhu, T., Song, H., Peng, R., Shi, Y., Qi, J., and Gao, G. F. (2017) Crystal structure of the Marburg virus nucleoprotein core domain chaperoned by a VP35 peptide reveals a conserved drug target for filovirus. *J. Virol.* **91,** e00996-17 CrossRef Medline
15. Aggarwal, M., Leser, G. P., Kors, C. A., and Lamb, R. A. (2018) Structure of the paramyxovirus parainfluenza virus 5 nucleoprotein in complex with an amino-terminal peptide of the phosphoprotein. *J. Virol.* **92,** e01304-17 CrossRef Medline
16. Renner, M., Bertinelli, M., Leyrat, C., Paesen, G. C., Saraiva de Oliveira, L. F., Huiskonen, J. T., and Grimes, J. M. (2016) Nucleocapsid assembly in pneumoviruses is regulated by conformational switching of the N protein. *eLife* **5,** e12627 CrossRef Medline
17. Galloux, M., Gabiane, G., Sourimant, J., Richard, C. A., England, P., Moudjou, M., Aumont-Nicaise, M., Fix, J., Rameix-Welti, M. A., and Eléouët, J. F. (2015) Identification and characterization of the binding site of the respiratory syncytial virus phosphoprotein to RNA-free nucleoprotein. *J. Virol.* **89,** 3484–3496 CrossRef Medline
18. Pereira, N., Cardone, C., Lassoued, S., Galloux, M., Fix, J., Assrir, N., Lescop, E., Bontems, F., Eléouët, J. F., and Sizun, C. (2017) New insights into structural disorder in human respiratory syncytial virus phosphoprotein and implications for binding of protein partners. *J. Biol. Chem.* **292,** 2120–2131 CrossRef Medline
19. El Omari, K., Scott, K., Dhaliwal, B., Ren, J., Abrescia, N. G. A., Budworth, J., Lockyer, M., Powell, K. L., Hawkins, A. R., and Stammers, D. K. (2008) Crystallization and preliminary X-ray analysis of the human respiratory syncytial virus nucleocapsid protein. *Acta Crystallogr. Sect. F Struct. Biol. Cryst. Commun.* **64,** 1019–1023 CrossRef Medline
20. Shapiro, A. B., Gao, N., O'Connell, N., Hu, J., Thresher, J., Gu, R. F., Overman, R., Hardern, I. M., and Sproat, G. G. (2014) Quantitative investigation of the affinity of human respiratory syncytial virus phosphoprotein C-terminus binding to nucleocapsid protein. *Virol. J.* **11,** 191 CrossRef Medline
21. Tawar, R. G., Duquerroy, S., Vonrhein, C., Varela, P. F., Damier-Piolle, L., Castagné, N., MacLellan, K., Bedouelle, H., Bricogne, G., Bhella, D., Eléouët, J. F., and Rey, F. A. (2009) Crystal structure of a nucleocapsid-like nucleoprotein-RNA complex of respiratory syncytial virus. *Science* **326,** 1279–1283 CrossRef Medline
22. Tran, T. L., Castagné, N., Dubosclard, V., Noinville, S., Koch, E., Moudjou, M., Henry, C., Bernard, J., Yeo, R. P., and Eléouët, J. F. (2009) The respiratory syncytial virus M2–1 protein forms tetramers and interacts with RNA and P in a competitive manner. *J. Virol.* **83,** 6363–6374 CrossRef Medline
23. Galloux, M., Tarus, B., Blazevic, I., Fix, J., Duquerroy, S., and Eléouët, J. F. (2012) Characterization of a viral phosphoprotein binding site on the surface of the respiratory syncytial nucleoprotein. *J. Virol.* **86,** 8375–8387 CrossRef Medline
24. García, J., García-Barreno, B., Vivo, A., and Melero, J. A. (1993) Cytoplasmic inclusions of respiratory syncytial virus-infected cells: formation of inclusion bodies in transfected cells that coexpress the nucleoprotein, the phosphoprotein, and the 22K protein. *Virology* **195,** 243–247 CrossRef Medline
25. García-Barreno, B., Delgado, T., and Melero, J. A. (1996) Identification of protein regions involved in the interaction of human respiratory syncytial virus phosphoprotein and nucleoprotein: Significance for nucleocapsid assembly and formation of cytoplasmic inclusions. *J. Virol.* **70,** 801–808 Medline
26. Rincheval, V., Lelek, M., Gault, E., Bouillier, C., Sitterlin, D., Blouquit-Laye, S., Galloux, M., Zimmer, C., Eleouet, J. F., and Rameix-Welti, M. A. (2017) Functional organization of cytoplasmic inclusion bodies in cells infected by respiratory syncytial virus. *Nat. Comm.* **8,** 563 CrossRef Medline
27. Uesugi, M., Nyanguile, O., Lu, H., Levine, A. J., and Verdine, G. L. (1997) Induced α helix in the VP16 activation domain upon binding to a human TAF. *Science* **277,** 1310–1313 CrossRef Medline
28. Chenavas, S., Estrozi, L. F., Slama-Schwok, A., Delmas, B., Di Primo, C., Baudin, F., Li, X., Crépin, T., and Ruigrok, R. W. (2013) Monomeric nucleoprotein of influenza A virus. *PLoS Pathog.* **9,** e1003275 CrossRef Medline
29. Castel, G., Chtéoui, M., Caignard, G., Préhaud, C., Méhouas, S., Réal, E., Jallet, C., Jacob, Y., Ruigrok, R. W., and Tordo, N. (2009) Peptides that mimic the amino-terminal end of the rabies virus phosphoprotein have antiviral activity. *J. Virol.* **83,** 10808–10820 CrossRef Medline
30. Bird, G. H., Boyapalle, S., Wong, T., Opoku-Nsiah, K., Bedi, R., Crannell, W. C., Perry, A. F., Nguyen, H., Sampayo, V., Devareddy, A., Mohapatra, S., Mohapatra, S. S., and Walensky, L. D. (2014) Mucosal delivery of a double-stapled RSV peptide prevents nasopulmonary infection. *J. Clin. Invest.* **124,** 2113–2124 CrossRef Medline
31. Gaillard, V., Galloux, M., Garcin, D., Eléouët, J. F., Le Goffic, R., Larcher, T., Rameix-Welti, M. A., Boukadiri, A., Héritier, J., Segura, J. M., Baechler, E., Arrell, M., Mottet-Osman, G., and Nyanguile, O. (2017) A short double-stapled peptide inhibits respiratory syncytial virus entry and spreading. *Antimicrob. Agents Chemother.* **61,** e02241-16 CrossRef Medline
32. Zarzycka, B., Kuenemann, M. A., Miteva, M. A., Nicolaes, G. A. F., Vriend, G., and Sperandio, O. (2016) Stabilization of protein-protein interaction complexes through small molecules. *Drug Discov. Today* **21,** 48–57 CrossRef Medline
33. Tran, T. L., Castagné, N., Bhella, D., Varela, P. F., Bernard, J., Chilmonczyk, S., Berkenkamp, S., Benhamo, V., Grznarova, K., Grosclaude, J., Nespoulos, C., Rey, F. A., and Eléouët, J. F. (2007) The nine C-terminal amino acids of the respiratory syncytial virus protein P are necessary and sufficient for binding to ribonucleoprotein complexes in which six ribonucleotides are contacted per N protein protomer. *J. Gen. Virol.* **88,** 196–206 CrossRef Medline
34. Fix, J., Galloux, M., Blondot, M. L., and Eléouët, J. F. (2011) The insertion of fluorescent proteins in a variable region of respiratory syncytial virus L polymerase results in fluorescent and functional enzymes but with reduced activities. *Open Virol. J.* **5,** 103–108 CrossRef Medline
35. Hardy, R. W., and Wertz, G. W. (1998) The product of the respiratory syncytial virus M2 gene ORF1 enhances readthrough of intergenic junctions during viral transcription. *J. Virol.* **72,** 520–526 Medline
36. Buchholz, U. J., Finke, S., and Conzelmann, K. K. (1999) Generation of bovine respiratory syncytial virus (BRSV) from cDNA: BRSV NS2 is not essential for virus replication in tissue culture, and the human RSV leader region acts as a functional BRSV genome promoter. *J. Virol.* **73,** 251–259 Medline
37. Chenal, A., Nizard, P., Forge, V., Pugnière, M., Roy, M. O., Mani, J. C., Guillain, F., and Gillet, D. (2002) Does fusion of domains from unrelated proteins affect their folding pathways and the structural changes involved in their function? A case study with the diphtheria toxin T domain. *Protein Eng.* **15,** 383–391 CrossRef Medline
38. Ortega, A., Amorós, D., and García de la Torre, J. (2011) Prediction of hydrodynamic and other solution properties of rigid proteins from atomic- and residue-level models. *Biophys. J.* **101,** 892–898 CrossRef Medline
39. Konarev, P. V., Volkov, V. V., Sokolova, A. V., Koch, M. H. J., and Svergun, D. I. (2003) PRIMUS: A Windows PC-based system for small-

angle scattering data analysis. *J. Appl. Crystallogr.* **36,** 1277–1282 CrossRef

40. Svergun, D. I. (1992) Determination of the regularization parameter in indirect-transform methods using perceptual criteria. *J. Appl. Crystallogr.* **25,** 495–503 CrossRef
41. Durand, D., Vivès, C., Cannella, D., Pérez, J., Pebay-Peyroula, E., Vachette, P., and Fieschi, F. (2010) NADPH oxidase activator p67(phox) behaves in solution as a multidomain protein with semi-flexible linkers. *J. Struct. Biol.* **169,** 45–53 CrossRef Medline
42. Petoukhov, M. V., Franke, D., Shkumatov, A. V., Tria, G., Kikhney, A. G., Gajda, M., Gorba, C., Mertens, H. D., Konarev, P. V., and Svergun, D. I. (2012) New developments in the ATSAS program package for small-angle scattering data analysis. *J. Appl. Crystallogr.* **45,** 342–350 CrossRef Medline